J. Fluid Mech. (2011), *vol.* 685, *pp.* 146–164. © Cambridge University Press 2011
doi:10.1017/jfm.2011.287

Evolution of vortex-surface fields in viscous Taylor–Green and Kida–Pelz flows

Yue Yang† and D. I. Pullin

Graduate Aerospace Laboratories, 205-45, California Institute of Technology, Pasadena, CA 91125, USA

(Received 23 January 2011; revised 22 June 2011; accepted 25 June 2011)

In order to investigate continuous vortex dynamics based on a Lagrangian-like formulation, we develop a theoretical framework and a numerical method for computation of the evolution of a vortex-surface field (VSF) in viscous incompressible flows with simple topology and geometry. Equations describing the continuous, timewise evolution of a VSF from an existing VSF at an initial time are first reviewed. Non-uniqueness in this formulation is resolved by the introduction of a pseudo-time and a corresponding pseudo-evolution in which the evolved field is 'advected' by frozen vorticity onto a VSF. A weighted essentially non-oscillatory (WENO) method is used to solve the pseudo-evolution equations in pseudo-time, providing a dissipative-like regularization. Vortex surfaces are then extracted as iso-surfaces of the VSFs at different real physical times. The method is applied to two viscous flows with Taylor–Green and Kida–Pelz initial conditions respectively. Results show the collapse of vortex surfaces, vortex reconnection, the formation and roll-up of vortex tubes, vorticity intensification between anti-parallel vortex tubes, and vortex stretching and twisting. A possible scenario for understanding the transition from a smooth laminar flow to turbulent flow in terms of topology of vortex surfaces is discussed.

Key words: topological fluid dynamics, turbulence theory, vortex dynamics

1. Introduction

Conceptual vortex tubes and sheets have long been utilized as basic vortical structures or elements of the vortex-dynamic paradigm in fluid mechanics (e.g. Batchelor 1967; Saffman 1992). In particular, intermittency in high-Reynolds-number turbulence has been hypothesized to be related to the organized vortical structures with candidate tube-like or sheet-like geometries (see Pullin & Saffman 1998). In a general sense, an open or closed 'vortex surface' can be defined as a smooth surface or manifold embedded within a three-dimensional velocity field, which has the property that the local vorticity vector is tangent at every point on the surface. Although coherent bundles of vortex lines with strong vorticity and tube-like geometry have been observed (e.g. She, Jackson & Orszag 1990; Jimenez *et al.* 1993) and analysed (see Constantin, Procaccia & Segel 1995) in turbulence, the existence of globally smooth vortex surfaces in general three-dimensional flows remains an open problem. Within the Clebsch representation (see Lamb 1932; Truesdell 1954), Yang & Pullin (2010) defined a vortex-surface field (VSF) as a smooth scalar field whose iso-surfaces

† Email address for correspondence: yy@caltech.edu

are vortex surfaces. They developed VSFs for both initial Taylor–Green (TG) (see Taylor & Green 1937; Brachet *et al.* 1983) and Kida–Pelz (KP) (see Kida 1985; Boratav & Pelz 1994) velocity fields which display simple topology and geometry.

For strictly inviscid barotropic flow with conservative body forces, the Helmholtz vorticity theorem shows that Lagrangian material surfaces or Lagrangian fields which are vortex surfaces or VSFs respectively at time $t = 0$, remain so for $t > 0$ (Helmholtz 1858; Yang & Pullin 2010). On the other hand, the breakdown of the frozen motion of vortex lines in viscous flow owing to violation of the Helmholtz theorem (e.g. Kida & Takaoka 1994; Chen *et al.* 2006) underscores a fundamental problem associated with identifying vortex surfaces at different times in real flows and turbulence in particular. This can perhaps be interpreted as the root cause of numerical obstacles in the implementation of Lagrangian formulations of Navier–Stokes dynamics (e.g. Ohkitani & Constantin 2003; Yang & Pullin 2010). Although a Lagrangian field evolving from a VSF initial condition can provide an interesting approximation to a VSF for a short period in high-Reynolds-number flows (Yang & Pullin 2010), it cannot be used to identify signature topological changes in vortex lines or surfaces, such as the vortex reconnection that is a crucial mechanism in turbulent transition and enstrophy generation (see Kida & Takaoka 1994).

In the present study, we consider VSF evolution in viscous incompressible flows for which initial VSFs exist. Our examples are TG and KP flows. The level sets of a VSF at different times will be shown to reveal vortex dynamics in the sense of the geometry and topology of vortex surfaces. We begin in § 2 by obtaining equations governing VSFs for viscous incompressible flows. In § 3, we develop the numerical methods used at present for computing VSF evolution. The convergence properties of the proposed numerical scheme is then analysed. The evolution of VSFs in both three-dimensional viscous TG and KP flows is presented in § 4 together with discussion of the corresponding vortex dynamics. Some conclusions are drawn in § 5.

2. Theoretical framework of the VSF

2.1. *Governing equations*

In a three-dimensional incompressible viscous flow, the velocity field is determined by the Navier–Stokes equations

$$\left.\begin{aligned} \frac{\partial \boldsymbol{u}}{\partial t} + \boldsymbol{u}\cdot\nabla\boldsymbol{u} &= -\frac{1}{\rho}\nabla p + \nu\nabla^2\boldsymbol{u}, \\ \nabla\cdot\boldsymbol{u} &= 0, \end{aligned}\right\} \tag{2.1}$$

with appropriate initial and boundary conditions, where $\boldsymbol{u}$ denotes the velocity field, p the pressure, ρ the density and ν the kinematic viscosity. The definition of a VSF $\phi_v(\boldsymbol{x}, t)$ requires that the cosine of the angle between the vorticity $\boldsymbol{\omega} \equiv \nabla \times \boldsymbol{u}$ and $\nabla\phi_v$ satisfies

$$\lambda_\omega \equiv \frac{\boldsymbol{\omega}\cdot\nabla\phi_v}{|\boldsymbol{\omega}||\nabla\phi_v|} = 0, \tag{2.2}$$

pointwise within the domain of interest for all time. If (2.2) holds uniformly within the domain at $t = 0$, then the temporal evolution of the VSF is described for $t \geqslant 0$ by

$$\frac{\mathrm{D}}{\mathrm{D}t}(\boldsymbol{\omega}\cdot\nabla\phi_v) = 0, \tag{2.3}$$

where the material derivative is defined as

$$\frac{\mathrm{D}}{\mathrm{D}t} \equiv \frac{\partial}{\partial t} + \boldsymbol{u} \cdot \boldsymbol{\nabla}. \tag{2.4}$$

From the equation of vorticity

$$\frac{\mathrm{D}\boldsymbol{\omega}}{\mathrm{D}t} = \boldsymbol{\omega} \cdot \boldsymbol{\nabla}\boldsymbol{u} + \nu \nabla^2 \boldsymbol{\omega} \tag{2.5}$$

and (2.3), Yang & Pullin (2010) obtained the equations governing the VSF ϕ_v as

$$\frac{\mathrm{D}\phi_v}{\mathrm{D}t} = \nu \mathscr{L}, \tag{2.6}$$

$$\boldsymbol{\nabla}\phi_v \cdot \nabla^2 \boldsymbol{\omega} + \boldsymbol{\omega} \cdot \boldsymbol{\nabla}\mathscr{L} = 0, \tag{2.7}$$

where $\mathscr{L}(\boldsymbol{x}, t)$ is assumed to be a regular scalar field. In principle, given the evolution of $\boldsymbol{u}$ and $\boldsymbol{\omega}$, one can solve (2.6) for ϕ_v, where, at each t, the function $\mathscr{L}$ is given by the solution of the hyperbolic partial differential equation (2.7). In Appendix C of Yang & Pullin (2010), it is shown that a necessary condition for the existence and uniqueness of solutions to equations of the type (2.7) is not satisfied (see Mingyu, Küpper & Masbaum 1997). Hence, this approach explicitly fails for the computation of VSF evolution in viscous flows $\nu > 0$. For inviscid flow $\nu = 0$, however, $\phi_v \equiv \phi$, where ϕ is a Lagrangian field satisfying

$$\frac{\mathrm{D}\phi}{\mathrm{D}t} = 0. \tag{2.8}$$

If ϕ is a smooth VSF at $t = 0$ then (2.8) is the Helmholtz theorem and describes a unique evolution for $t > 0$.

2.2. *Restoration of uniqueness and approximate numerical solutions*

To restore uniqueness with $\nu > 0$ of VSF evolution from a given initial VSF, we introduce a time-like variable τ, with the dimension (time/length), and let $\phi_v(\boldsymbol{x}, t) = \phi_v(\boldsymbol{x}, t; \tau)$ and $\mathscr{L}(\boldsymbol{x}, t) = \mathscr{L}(\boldsymbol{x}, t; \tau)$. We seek solutions

$$\phi_v = \lim_{\tau \to \infty} \phi_v(\boldsymbol{x}, t; \tau) \quad \text{and} \quad \mathscr{L} = \lim_{\tau \to \infty} \mathscr{L}(\boldsymbol{x}, t; \tau), \tag{2.9}$$

where $\mathscr{L}(\boldsymbol{x}, t; \tau)$ satisfies

$$\frac{\mathrm{D}}{\mathrm{D}t}(\boldsymbol{\omega} \cdot \boldsymbol{\nabla}\phi_v) + \nu \frac{\partial \mathscr{L}}{\partial \tau} = 0, \tag{2.10}$$

for all $\boldsymbol{x}$ at fixed t. From (2.5), (2.6) and (2.10) it can be then be shown that

$$\frac{\mathscr{D}\mathscr{L}}{\mathscr{D}\tau} = -\boldsymbol{\nabla}\phi_v \cdot \nabla^2 \boldsymbol{\omega}, \tag{2.11}$$

where the left-hand side is expressed in terms of the pseudo-material-like derivative defined as

$$\frac{\mathscr{D}}{\mathscr{D}\tau} \equiv \frac{\partial}{\partial \tau} + \boldsymbol{\omega} \cdot \boldsymbol{\nabla} \tag{2.12}$$

based on the pseudo-time τ and the frozen vorticity $\boldsymbol{\omega}(\boldsymbol{x}, t)$ at fixed t.

Now consider

$$\frac{\mathscr{D}\phi_v}{\mathscr{D}\tau} = Q, \tag{2.13}$$

where Q is a function to be chosen subsequently. Differentiating (2.6) with respect to τ and (2.13) with respect to t and equating expressions for $\partial^2\phi_v(\boldsymbol{x}, t; \tau)/(\partial t\partial\tau)$ with $\partial\boldsymbol{u}(\boldsymbol{x}, t)/\partial\tau = 0$ then yields

$$\frac{\partial}{\partial t}(\boldsymbol{\omega}\cdot\boldsymbol{\nabla}\phi_v) + \nu\frac{\partial\mathscr{L}}{\partial\tau} = \frac{\partial Q}{\partial t} + \boldsymbol{u}\cdot\boldsymbol{\nabla}\left(\frac{\partial\phi_v}{\partial\tau}\right). \tag{2.14}$$

From the above and using (2.10) and (2.13), we can obtain

$$\frac{\mathrm{D}}{\mathrm{D}t}(\boldsymbol{\omega}\cdot\boldsymbol{\nabla}\phi_v) + \nu\frac{\partial\mathscr{L}}{\partial\tau} = \frac{\mathrm{D}Q}{\mathrm{D}t} = 0. \tag{2.15}$$

It seems that Q can be any Lagrangian field ϕ satisfying (2.8). In particular, we can choose $Q = 0$, and then (2.13) becomes

$$\frac{\mathscr{D}\phi_v}{\mathscr{D}\tau} \equiv \frac{\partial\phi_v}{\partial\tau} + \boldsymbol{\omega}\cdot\boldsymbol{\nabla}\phi_v = 0. \tag{2.16}$$

With $\boldsymbol{\omega}$ given at fixed t, (2.11) and (2.16) then define the evolution for $\tau > 0$ of $\phi_v(\boldsymbol{x}, t; \tau)$ and $\mathscr{L}(\boldsymbol{x}, t; \tau)$. Equation (2.16) states that ϕ_v is 'convected' along frozen (in τ) vortex lines, which are characteristics at fixed time t. We will subsequently demonstrate that this formulation, together with a suitable numerical method, provides a viable way to obtain approximate numerical solutions of (2.6) and (2.7). While it is expected that integration of (2.11) and (2.16) forward in τ could lead to exponentially small structures as $\tau \to \infty$ without diffusion terms, they have unique viscosity solutions (Crandall & Lions 1983) for given smooth initial conditions. In the sequel, it will be argued that use of a weighted essentially non-oscillatory (WENO) method will regularize both equations as

$$\frac{\mathscr{D}\mathscr{L}}{\mathscr{D}\tau} = -\boldsymbol{\nabla}\phi_v\cdot\nabla^2\boldsymbol{\omega} + \epsilon\nabla^2\mathscr{L}, \tag{2.17}$$

$$\frac{\mathscr{D}\phi_v}{\mathscr{D}\tau} = \epsilon\nabla^2\phi_v, \tag{2.18}$$

where $\epsilon(\boldsymbol{x}, t; \tau) \ll 1$ is an effective numerical diffusivity. At fixed t, the limit (2.9) can be obtained by solving (2.17) and (2.18) simultaneously. It remains to be demonstrated that this limit is 'steady' in τ.

3. Numerical overview

3.1. *Numerical methods*

The Navier–Stokes equations (2.1) in a periodic box of side 2π were computed by a standard pseudo-spectral method on a uniform grid N^3 for the Reynolds number $Re = 1/\nu$ in the period from $t = 0$ to $t = t_{max}$. The aliasing error was removed by use of a 16th-order exponential filter (Shu *et al.* 2005). The scalar equations (2.6) and (2.16) were advanced in t and τ respectively using the third-order total-variation-diminishing Runge–Kutta method and the convection terms were treated by the fifth-order WENO scheme (Jiang & Shu 1996). The time steps Δt and $\Delta\tau$ were chosen to ensure that the corresponding Courant–Friedrichs–Lewy (CFL) numbers

$$\mathrm{CFL}_t = \frac{\Delta t}{\Delta x}\max(|u_x|, |u_y|, |u_z|) \quad \text{and} \quad \mathrm{CFL}_\tau = \frac{\Delta\tau}{\Delta x}\max(|\omega_x|, |\omega_y|, |\omega_z|), \tag{3.1}$$

for (2.6) and (2.16) were 0.5 or less for numerical stability and accuracy, where $\Delta x = 2\pi/N$. It is noted that $\Delta\tau$ could be much less than Δt when $|\boldsymbol{\omega}| \gg |\boldsymbol{u}|$ at some time.

Run	TG1	TG2	TG3	TG4	TG5	KP1	KP2
Re	50	100	200	400	800	200	400
N^3	128^3	256^3	256^3	512^3	512^3	512^3	512^3
t_{max}	10	10	10	10	10	3	3

TABLE 1. Parameters of study for TG and KP flows.

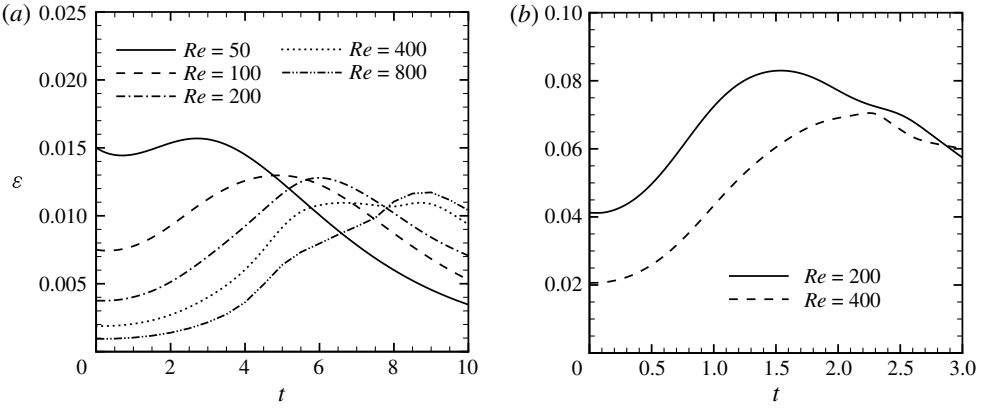

FIGURE 1. Dissipation rate: (*a*) TG flow, (*b*) KP flow.

For TG flows, the initial fields for (2.1) and (2.6) were chosen as

$$\boldsymbol{u}(\boldsymbol{x}, t = 0) = (\sin x \cos y \cos z, -\cos x \sin y \cos z, 0), \tag{3.2}$$

and

$$\phi_v(\boldsymbol{x}, t = 0) = (\cos 2x - \cos 2y) \cos z. \tag{3.3}$$

For KP flows, $\boldsymbol{u}(\boldsymbol{x}, t = 0)$ was given in Boratav & Pelz (1994) and $\phi_v(\boldsymbol{x}, t = 0)$ was obtained numerically in Yang & Pullin (2010) by an expansion based on optimal basis functions with the same octahedral symmetries as the KP initial field. In addition, the TG and KP symmetries (Brachet *et al.* 1983; Kida 1985) were utilized to reduce the computational time and scale. Parameters of the runs in the present study are listed in table 1. As shown in figure 1, the dissipation rate $\varepsilon = \nu\langle \boldsymbol{\nabla u} : \boldsymbol{\nabla u} \rangle$ in both flows increases at early time and approaches a peak after a finite time, which can indicate the transition from initial smooth flow to turbulent flow at high Reynolds numbers (Brachet *et al.* 1983; Boratav & Pelz 1994).

3.2. *Numerical implementation for computing the VSF*

The exact solution of the VSF satisfies (2.2) for all time. However, it appears that $|\boldsymbol{\nabla}\phi_v|$ tends to become unbounded for long times in evolution even from a smooth initial field (Yang & Pullin 2010). In other words, we might not be able to find a globally smooth ϕ_v with a finite resolution for all time. Hence, we introduce a filtering or artificial dissipation mechanism for a smooth VSF in the evolution and at the same time keep the volume averaged $\langle|\lambda_\omega|\rangle$ as small as possible. It is noted that the implicit numerical viscosity in the finite-difference WENO scheme can keep $|\boldsymbol{\nabla}\phi_v|$ finite as shown in (2.18), where $\epsilon = \epsilon_{WENO}(\boldsymbol{x}, t; \tau)$ depends on the smoothness of the discretized

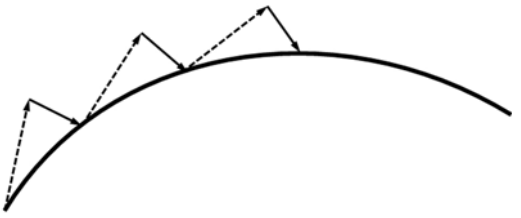

FIGURE 2. Sketch of the numerical implementation for computing the VSF. Solid curve, solution of the VSF; dashed arrow, prediction step (3.4); solid arrow, correction step (3.5).

local ϕ_v that is determined by the local $\nabla\phi_v$ and resolution N (see Jiang & Shu 1996). Here, ϵ_{WENO} is negligible where ϕ_v is smooth, which avoids unnecessary numerical diffusion in smooth regions. As an alternative to WENO, other regularization methods, for example using an explicit numerical viscosity or a subgrid scale model for the diffusion term, could also be useful for the solution of (2.18) with finite resolution, but these have not yet been explored.

In the implementation, we solved (2.1) and (2.6) with $\mathscr{L} = 0$ simultaneously in time t. For each time step, only (2.18) was computed for a period T_τ in the pseudo-time τ to implicitly determine the approximate $\mathscr{L}$ in (2.7) by (2.15), rather than solving (2.17) and (2.18) simultaneously. This approach has the advantage that discretized errors for the term $\nabla\phi_v \cdot \nabla^2\boldsymbol{\omega}$ with high-order derivatives in (2.17) are avoided. Therefore, within a single time step the VSF was computed as

$$\frac{\partial\phi_v^*(\boldsymbol{x},t)}{\partial t} + \boldsymbol{u}(\boldsymbol{x},t)\cdot\nabla\phi_v^*(\boldsymbol{x},t) = \epsilon_{WENO}(\boldsymbol{x},t)\nabla^2\phi_v^*(\boldsymbol{x},t), \quad t \geqslant 0, \tag{3.4}$$

and then at fixed time t, the temporary VSF ϕ_v^* is transported along the frozen vorticity field in the pseudo-time τ as

$$\frac{\partial\phi_v(\boldsymbol{x},t;\tau)}{\partial\tau} + \boldsymbol{\omega}(\boldsymbol{x},t)\cdot\nabla\phi_v(\boldsymbol{x},t;\tau) = \epsilon_{WENO}(\boldsymbol{x},t;\tau)\nabla^2\phi_v(\boldsymbol{x},t;\tau), \quad 0 \leqslant \tau \leqslant T_\tau, \tag{3.5}$$

with

$$\phi_v(\boldsymbol{x},t;\tau=0) = \phi_v^*(\boldsymbol{x},t), \tag{3.6}$$

to obtain the approximate solution for (2.9). Finally, $\phi_v^*(\boldsymbol{x},t)$ in (3.4) is updated by $\phi_v(\boldsymbol{x},t;\tau=T_\tau)$ for every time step. Here, (3.4) serves as the prediction step and (3.5) as the correction or projection step as sketched in figure 2.

3.3. *Convergence of numerical solutions*

For a fixed time t, finite $\langle|\lambda_\omega|\rangle$ could be generated in (3.4) because of the deviation between the temporary scalar field ϕ_v^* and the VSF ϕ_v, while $\langle|\lambda_\omega|\rangle$ can be reduced by using (3.5). Next we will analyse the convergence of the correction step (3.5) onto the approximate VSF.

Using (2.18) and $\partial\boldsymbol{\omega}(\boldsymbol{x},t)/\partial\tau = 0$ at fixed t, and following a line of analysis applied in Yang, Pullin & Bermejo-Moreno (2010) and Yang & Pullin (2010) to a Lagrangian field, we can show, after some algebra, that

$$\frac{\mathscr{D}|\nabla\phi_v|}{\mathscr{D}\tau} = \frac{1}{|\nabla\phi_v|}(-(\nabla\phi_v\cdot\boldsymbol{S}_\omega\cdot\nabla\phi_v) + \epsilon\nabla\phi_v\cdot\nabla^2\nabla\phi_v), \tag{3.7}$$

$$\frac{\mathscr{D}}{\mathscr{D}\tau}(\boldsymbol{\omega}\cdot\nabla\phi_v) = \epsilon\boldsymbol{\omega}\cdot\nabla^2\nabla\phi_v. \tag{3.8}$$

The equation of λ_ω, the cosine of the angle between $\boldsymbol{\omega}$ and $\nabla\phi_v$ as a function of the pseudo-time τ, can then be obtained as

$$\frac{\mathscr{D}\lambda_\omega}{\mathscr{D}\tau} = \mathscr{A}\lambda_\omega + \mathscr{B}, \tag{3.9}$$

with

$$\mathscr{A}(\boldsymbol{x}, \tau) = \boldsymbol{n}_v \cdot \boldsymbol{S}_\omega \cdot \boldsymbol{n}_v - \boldsymbol{n}_\omega \cdot \nabla|\boldsymbol{\omega}| - \epsilon R_\Phi \boldsymbol{n}_v \cdot \boldsymbol{n}_\Phi, \tag{3.10}$$

$$\mathscr{B}(\boldsymbol{x}, \tau) = \epsilon R_\Phi \boldsymbol{n}_\omega \cdot \boldsymbol{n}_\Phi, \tag{3.11}$$

where the symmetric part of the vorticity-gradient tensor $\boldsymbol{S}_\omega$ has entries $S_{\omega,ij} = (1/2)(\partial\omega_i/\partial x_j + \partial\omega_j/\partial x_i)$, and unit vectors and a dimensionless ratio are respectively

$$\boldsymbol{n}_\omega = \frac{\boldsymbol{\omega}}{|\boldsymbol{\omega}|}, \quad \boldsymbol{n}_v = \frac{\nabla\phi_v}{|\nabla\phi_v|}, \quad \boldsymbol{n}_\Phi = \frac{\nabla^2\nabla\phi_v}{|\nabla^2\nabla\phi_v|}, \quad R_\Phi = \frac{|\nabla^2\nabla\phi_v|}{|\nabla\phi_v|}. \tag{3.12}$$

Since $\nabla \cdot \boldsymbol{\omega} = 0$, the eigenvalues of $\boldsymbol{S}_\omega$ satisfy $\Gamma_\alpha + \Gamma_\beta + \Gamma_\gamma = 0$. By analogy with the analysis in Yang *et al.* (2010), we then expect that $\nabla\phi_v$ will tend to align with eigenvectors of $\boldsymbol{S}_\omega$ with negative eigenvalues, i.e. the local compressive strain rates of the vorticity field. Since there is no preferred alignment between $\boldsymbol{n}_\omega$ and $\nabla|\boldsymbol{\omega}|$, the leading term $\langle \boldsymbol{n}_v \cdot \boldsymbol{S}_\omega \cdot \boldsymbol{n}_v \rangle$ in $\langle\mathscr{A}\rangle$ should be statistically negative. This suggests that the solution of (2.18) will take the form

$$\langle|\lambda_\omega(t, \tau)|\rangle \sim \langle|\lambda_\omega(t, \tau = 0)|\rangle \exp(\langle\mathscr{A}\rangle\tau) + O(\epsilon R_\Phi), \quad 0 \leqslant \tau \leqslant T_\tau. \tag{3.13}$$

3.4. *Numerical experiments on the convergence of numerical solutions*

Using the initial condition given by an exact VSF (3.3), the temporal evolution of $\langle|\lambda_\omega|\rangle$ in the TG flow for $Re = 100$ and $N = 256$ is shown in figure 3(*a*). At fixed t, we find that $\langle|\lambda_\omega|\rangle$ decreases to a small value with increasing computational period T_τ for (3.5) obtained by increasing $N_\tau = T_\tau/\Delta t$. We define the L_∞ error norm $\|\langle|\lambda_\omega|\rangle\|_\infty$ as the maximum value of $\langle|\lambda_\omega|\rangle$ in the evolution of ϕ_v from $t = 0$ to $t = t_{max}$. Figure 3(*b*) shows the effect of the resolution N on the convergence of the VSF solution in N_τ. For an initial ϕ_v with a finite $\langle|\lambda_\omega|\rangle$, the solution of (3.9) appears to show exponential decay for small τ, but this trend is mitigated by the inhomogeneous term $\mathscr{B} \sim O(\epsilon R_\Phi)$ in (3.9) controlled by the numerical viscosity at late τ. As a result, we can see that smaller $\|\langle|\lambda_\omega|\rangle\|_\infty$ for the same N_τ are obtained in the runs with larger N, because the numerical viscosity ϵ_{WENO} is reduced by increasing grid resolution (see Jiang & Shu 1996). This implies a longer period with rapid decay dominated by the first term in the right-hand side of (3.13), because the inhomogeneous term $O(\epsilon R_\Phi)$ is reduced. For larger Reynolds numbers, it is expected that higher resolution is required to achieve similar convergence within a finite T_τ.

The time history of $\langle|\lambda_\omega|\rangle$ in TG and KP flows at different Reynolds numbers is shown in figure 4, where $N_\tau = 50$ for all runs and values of N are used as listed in table 1. These are chosen to ensure that the maximum $\|\langle|\lambda_\omega|\rangle\|_\infty \approx 0.03$ which is equivalent to 3 % of the possible maximum $|\lambda_\omega|$. For comparison, also displayed in figure 4 are temporal evolutions of $\langle|\lambda_\omega|\rangle$ for Lagrangian fields ϕ governed by (2.8) with the same initial conditions for the VSF simulations. The increase in $\langle|\lambda_\omega|\rangle$ with

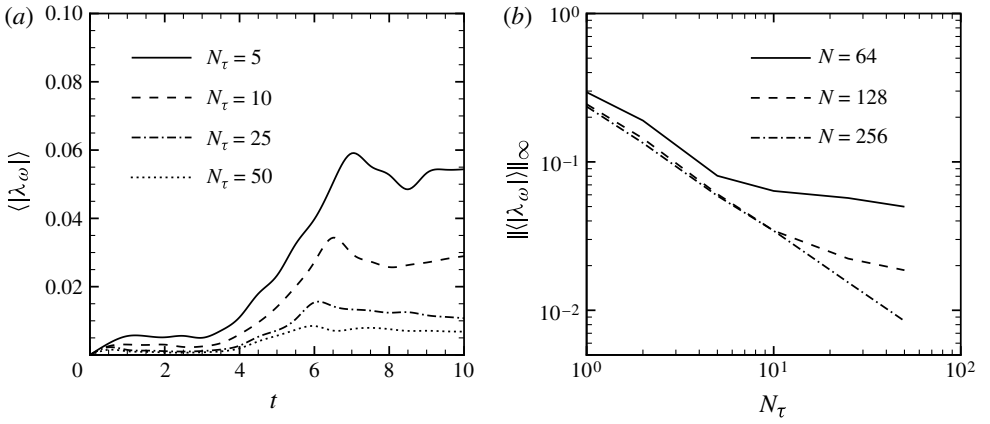

FIGURE 3. Convergence studies of the numerical solutions for the VSF in the TG flow at $Re = 100$: (*a*) temporal evolution of $\langle|\lambda_\omega|\rangle$, $N = 256$, (*b*) dependence of $\|\langle|\lambda_\omega|\rangle\|_\infty$ on N and N_τ.

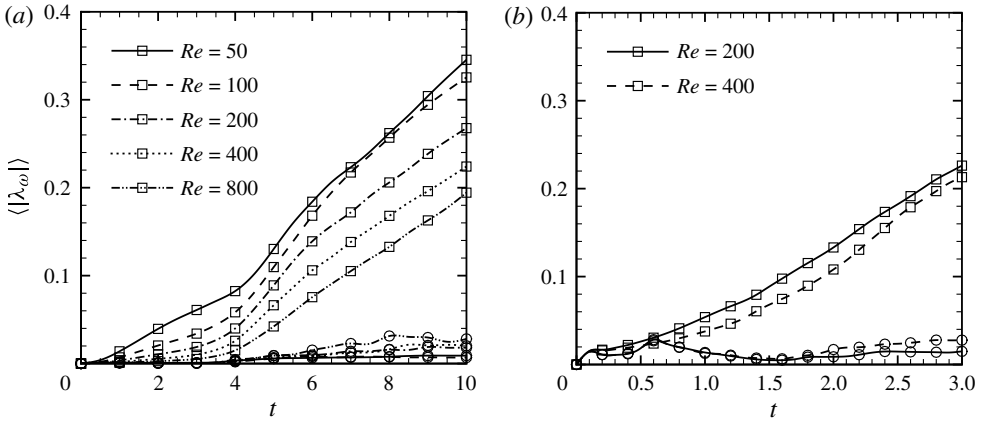

FIGURE 4. Temporal evolution of $\langle|\lambda_\omega|\rangle$ in TG and KP flows at different Reynolds numbers (□, Lagrangian field with the initial VSF; ○: VSF), (*a*) TG flow, (*b*) KP flow.

time in the evolution of Lagrangian fields occurs because the Helmholtz vorticity theorem is violated for viscous flow (Yang & Pullin 2010). In contrast, $\langle|\lambda_\omega|\rangle$ in the VSF simulations are substantially reduced by solving (3.4) and (3.5).

4. Application to viscous Taylor–Green and Kida–Pelz flows

4.1. *Evolution of VSFs in TG flows*

4.1.1. *Geometry and topology of vortex surfaces and lines in evolution*

The temporal evolution of vortex surfaces obtained from the VSF ϕ_v in the TG flow at $Re = 400$ within the periodic domain $0 \leqslant x, y, z \leqslant 2\pi$ is shown in figure 5. Vortex surfaces can be extracted as iso-surfaces of the VSFs at different times. The scaled contour levels are defined as $\hat{\phi}_v \equiv \phi_v/|\phi_v|_{max}$ with $-1 \leqslant \hat{\phi}_v \leqslant 1$. Colour on the extracted vortex surfaces is rendered by $0 \leqslant |\boldsymbol{\omega}| \leqslant 12$ from blue to red. We remark that since ϕ_v is not conserved in the evolution, its range may change as a result of

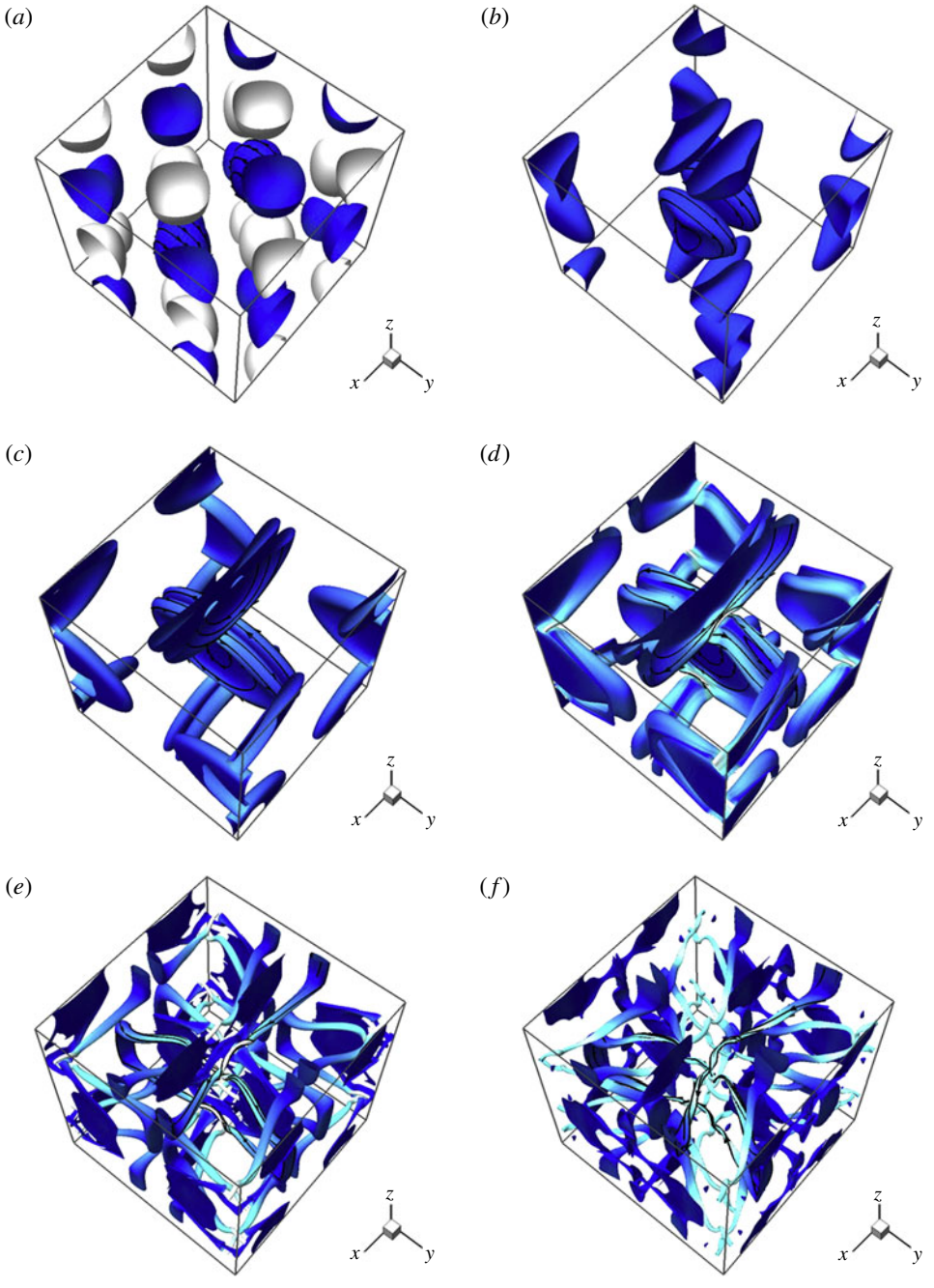

FIGURE 5. (Colour online available at journals.cambridge.org/flm) Evolution of vortex surfaces in the TG flow at $Re = 400$. Some vortex lines are integrated and plotted on the iso-surfaces of $\hat{\phi}_v$. Colour on the surfaces is rendered by $0 \leqslant |\boldsymbol{\omega}| \leqslant 12$ from dark to light. The iso-surfaces of ϕ_v at negative contour levels are not shown for clarity except in figure 5(*a*): (*a*) $t = 0$, $\hat{\phi}_v = 0.5$ (blue) and -0.5 (white), (*b*) $t = 1.5$, $\hat{\phi}_v = 0.5$, (*c*) $t = 3$, $\hat{\phi}_v = 0.5$, (*d*) $t = 4.5$, $\hat{\phi}_v = 0.5$, (*e*) $t = 5$, $\hat{\phi}_v = 0.5$, (*f*) $t = 7$, $\hat{\phi}_v = 0.45$.

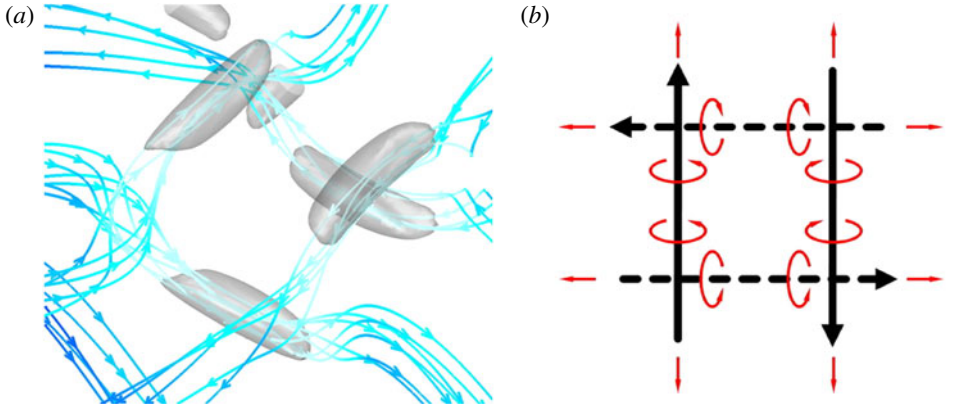

FIGURE 6. (Colour online) Interacting vortex lines on the tube-like vortex surfaces at $t = 5$ in the TG flow at $Re = 400$ in figure 5(*e*). The rapid local intensification of the vorticity could be explained by the interaction of anti-parallel vortex tubes and the Biot–Savart law. (*a*) Typical vortex lines with strong vorticity and iso-surfaces of $|\boldsymbol{\omega}|$ at $0.8|\boldsymbol{\omega}|_{max}$ (translucent grey surfaces). Colour on the lines is rendered by $0 \leqslant |\boldsymbol{\omega}| \leqslant 12$ from dark to light. (*b*) Configuration of the intensification of vortex lines (solid lines at the top and dashed lines at the bottom, induced velocity shown in red arrows).

numerical dissipation in (3.4) and (3.5). Some vortex lines are integrated from points on the iso-surfaces of ϕ_v. We can see that all lie almost on the vortex surfaces owing to very small $\langle|\lambda_\omega|\rangle$ in the simulation.

As shown in figure 5(*a*), all the closed and unknotted vortex lines have the same direction on each surface. Here, the iso-surfaces of ϕ_v at negative contour levels are not shown for clarity except in figure 5(*a*). It is noted that all the surfaces at particular contour levels $\hat{\phi}_v = \pm C$ have the same dynamics but they move in different directions under the TG symmetries (Brachet *et al.* 1983). In figures 5(*b*) and 5(*c*), the vortex surfaces are stretched and gradually approach to each other, but the topology of both the vortex surfaces and vortex lines on the surfaces is unchanged. In figure 5(*d*), incipient vortex reconnection, which is usually characterized by topological changes of vortex lines and surfaces (see Kida & Takaoka 1994), appears to begin at impermeable planes (e.g. $x = \pi$) (Brachet *et al.* 1983) and junctions between anti-parallel vortex surfaces roughly from $t = 4$ to $t = 5$. Just prior to reconnection the directions of vortex lines on neighbouring vortex surfaces (see figure 5*c*) are opposite, indicating that reconnection at the impermeable faces is the result of a simple vorticity cancellation as sketched in figure 3(*a*) in Kida & Takaoka (1994).

In figure 5(*e*), vortex tubes (actually vortex rings in the whole periodic domain) are rolled up at the edges of vortex surfaces around $t = 5$. We can see that significant vorticity intensification occurs near the joint of anti-parallel vortex tubes (e.g. Siggia 1985; Kerr 1993). Based on the directionality of vorticity on these tubes in figure 6(*a*) combined with qualitative interpretation of the Biot–Savart law, we conclude that the vortex tubes, exhibiting a high-degree of symmetry, are stretched by the induced velocity from neighbouring ones as sketched in figure 6(*b*).

In addition, the vortex tubes appear to be twisted and flattened either by self-induced dynamics or interaction with others. Figure 5(*f*) shows a tangle of interacting vortex tubes or ribbons at a late time $t = 7$. To illustrate the full complexity of vortex surfaces for the TG flow, figure 7 shows iso-contour levels at $t = 7$ with both signs.

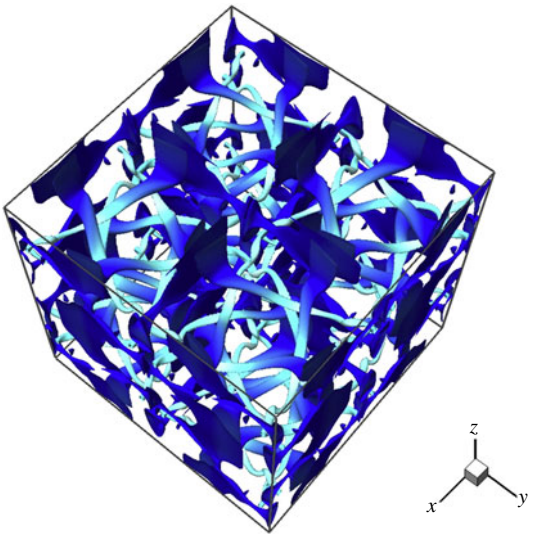

FIGURE 7. (Colour online) Vortex surfaces showing iso-surfaces of the VSF with both signs ($\hat{\phi}_v = \pm 0.45$) in the TG flow for $Re = 400$ at $t = 7$.

The geometry of figures 5(*f*) and 7 may be interpreted as exemplifying a common archetypal picture of turbulence in terms of vortices or vortex tubes. To obtain the VSF at a full turbulent-like state with the Kolmogorov five-third scaling of the velocity spectrum, we would need to simulate the TG flow for $Re \geqslant 1600$ at $t = 8{\sim}9$ (Brachet *et al.* 1983). The resolution for the corresponding VSF simulation with an acceptably small $\langle|\lambda_\omega|\rangle$ would be $N^3 = 2048^3$ or higher with $N_\tau = 50$.

4.1.2. *Vortex surfaces and other iso-surfaces*

For comparison with vortex surfaces, the evolution of iso-surfaces of $|\boldsymbol{\omega}|$, which was investigated by Brachet *et al.* (1983), is shown in figure 8, where the scaled contour levels $\hat{\omega} \equiv |\boldsymbol{\omega}|/|\boldsymbol{\omega}|_{max}$ were selected to show the structures at intermediate scales. In general, the iso-surface geometry of $|\boldsymbol{\omega}|$ does not resemble that of ϕ_v in figure 5 at the same time, and the vortex lines are clearly not attached on the iso-surfaces of $|\boldsymbol{\omega}|$ in figure 8, which indicates perhaps that the iso-surfaces of $|\boldsymbol{\omega}|$ are not a good approximation to vortex surfaces. Nonetheless the evolution of Eulerian vortical structures in figure 8 also shows the flattening process up to about $t = 3$, perhaps the rolling-up of vortex sheets at $t = 5$, and disordered patches at $t = 7$ (Brachet *et al.* 1983). This shows some qualitative similarity with corresponding observations of vortex surfaces in figure 5. Moreover, it appears that vortex lines with strong vorticity tend to be organized in tubes or ribbons (e.g. She *et al.* 1990; Jimenez *et al.* 1993), so the iso-surfaces of very high $|\boldsymbol{\omega}|$ may be close to some segments of vortex surfaces as shown in figure 6(*a*).

It may also be of interest to consider other Eulerian measures of vortex structure. Iso-surfaces of the intermediate eigenvalue λ_2 (Jeong & Hussain 1995) of $\boldsymbol{S}^2 + \boldsymbol{\Omega}^2$ are shown at two times in figure 9, where $\boldsymbol{S}$ and $\boldsymbol{\Omega}$ are respectively the symmetric and antisymmetric parts of the velocity gradient tensor $\boldsymbol{\nabla u}$. Again these do not resemble visually the vortex surfaces in figure 5 at similar times. In contrast, at $t = 7$, iso-surfaces of both $|\boldsymbol{\omega}|$ and λ_2 produce visually similar structures in figures 8(*f*) and 9(*b*) respectively.

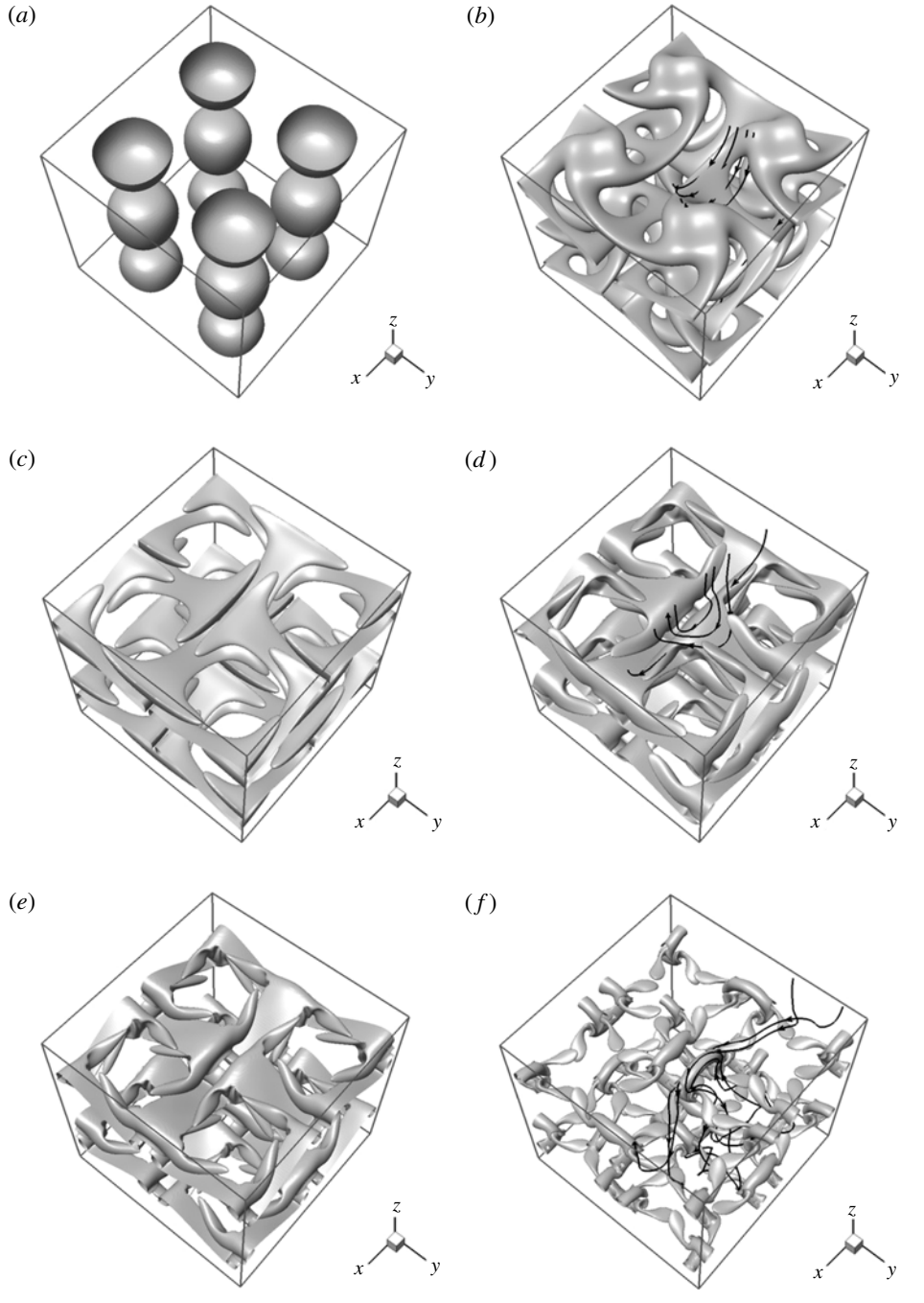

FIGURE 8. Evolution of iso-surfaces of the vorticity magnitude $|\boldsymbol{\omega}|$ in the TG flow at $Re = 400$. Some vortex lines are integrated from points on the iso-surfaces at $t = 1.5$, 4.5 and 7: (*a*) $t = 0$, $\hat{\omega} = 0.6$, (*b*) $t = 1.5$, $\hat{\omega} = 0.9$, (*c*) $t = 3$, $\hat{\omega} = 0.6$, (*d*) $t = 4.5$, $\hat{\omega} = 0.2$, (*e*) $t = 5$, $\hat{\omega} = 0.2$, (*f*) $t = 7$, $\hat{\omega} = 0.6$.

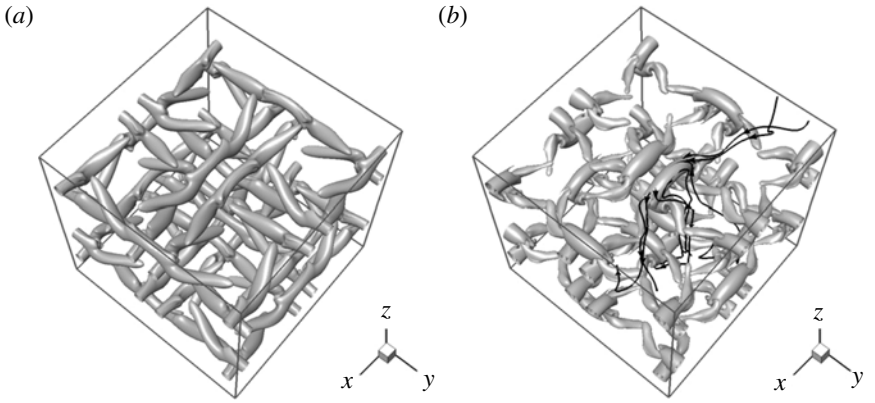

FIGURE 9. Iso-surfaces of λ_2 in the TG flow at $Re = 400$. Some vortex lines are integrated from points on the iso-surfaces at $t = 7$: (*a*) $t = 5$, (*b*) $t = 7$.

It is difficult, however, to elucidate the underlying dynamics of vortex lines or surfaces, e.g. vortex stretching and twisting, from Eulerian structures. In particular, the reconnections of vortex surfaces and iso-surfaces of $|\boldsymbol{\omega}|$ should be considered separately (Kida & Takaoka 1994). The significant topological changes of iso-surfaces of $|\boldsymbol{\omega}|$ from $t = 0$ to $t = 3$ in figure 8(*a–c*) cannot be interpreted in terms of the topology of vortex lines or surfaces in figure 5(*a–c*). On the other hand, the reconnection of vortex surfaces shown in figure 5(*d*) is not observed by iso-surfaces of $|\boldsymbol{\omega}|$ in figure 8(*d*). Compared with the Eulerian vortical structures, the detailed evolution of vortex lines and surfaces may be helpful in understanding the mechanisms of vortex reconnection such as viscous cancellation (see figure 5*c*,*d*) and bridging (e.g. Kida, Takaoka & Hussain 1991; Hussain & Duraisamy 2011).

4.1.3. *Effects of the Reynolds number and initial condition*

Using results obtained from simulations listed in table 1, we find that vortex surfaces at different Reynolds numbers appear to have similar topology and evolutionary geometries in $0 \leqslant t \leqslant 3$. However, as shown in figure 10, the rolling-up of vortex tubes around $t = 5$ observed for all simulations with $Re \geqslant 100$ is not seen in the low-Reynolds-number TG flow at $Re = 50$.

This suggests that the tube-rolling event is a dynamical requirement for the transition from a smooth velocity field to turbulence in the TG flow. From $t = 4$ to $t = 8$, the vortex surfaces at $Re = 200$ to $Re = 800$ appear to have the same topology while the geometry of vortex surfaces in high-Re flows is more complicated than that in low-Re flows. For instance, the vortex surfaces for TG flow at $Re = 400$ and $Re = 800$ are compared at $t = 7.5$ in figure 11. We can see that the vortex tubes at $Re = 800$ show more obvious helical geometry (e.g. Ricca 1994; Fukumoto & Okulov 2005), which can generate more intense small-scale velocity fields, than that at $Re = 400$.

Moreover, the statistical geometry of Lagrangian structures at late times appears to be insensitive to their initial shapes in isotropic turbulence (Yang *et al.* 2010) and turbulent channel flow (Yang & Pullin 2011). Likewise, as shown in figure 12(*a–c*), the VSFs obtained by evolution from independent initial VSFs ϕ_0, such as (3.3), $\phi_0 = \cos x \cos y \cos z$, and $\phi_0 = \cos x \cos^3 y \cos^2 z$, produce quite similar vortex-surface geometry in the same TG flow at the same time $t = 7.5$. Additionally, as illustrated in

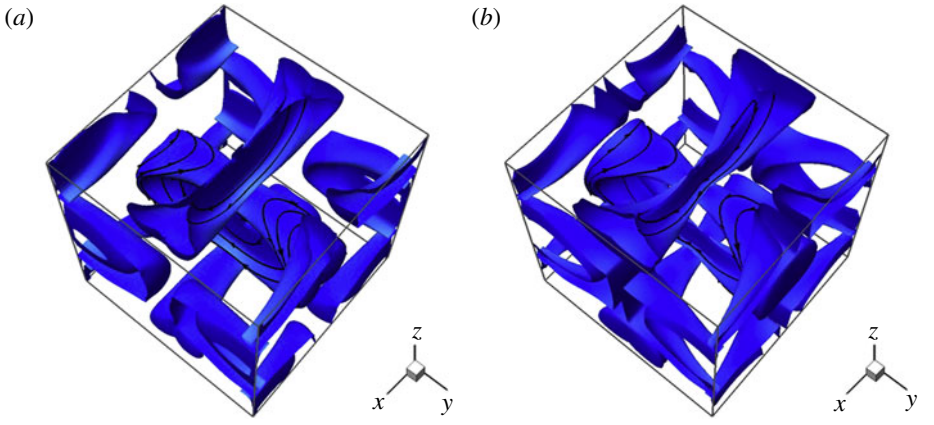

FIGURE 10. (Colour online) Evolution of vortex surfaces in the TG flow at $Re = 50$. Some vortex lines are integrated and plotted on the iso-surfaces at $\hat{\phi}_v$. Colour on the surfaces is rendered by $0 \leqslant |\boldsymbol{\omega}| \leqslant 12$ from dark to light: (*a*) $t = 5$, $\hat{\phi}_v = 0.5$, (*b*) $t = 6$, $\hat{\phi}_v = 0.5$.

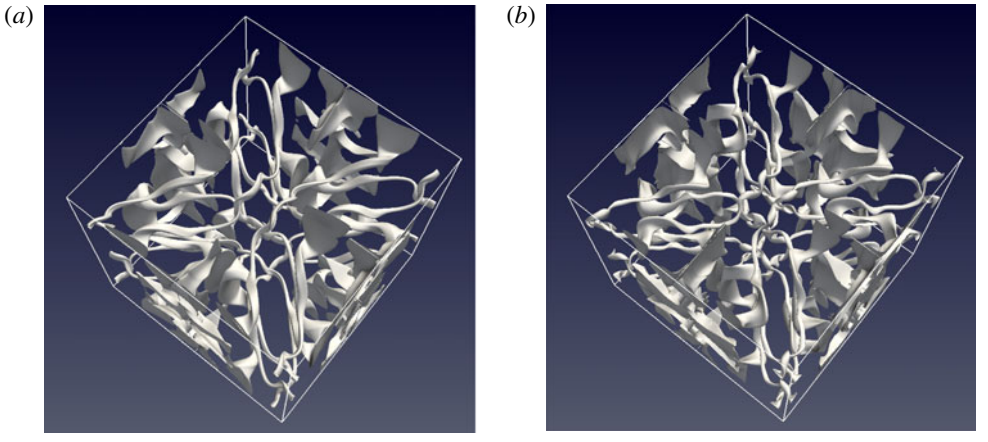

FIGURE 11. (Colour online) Vortex surfaces in TG flows for different Reynolds numbers at $t = 7.5$: (*a*) $Re = 400$, (*b*) $Re = 800$.

figure 12(*d*), the present VSF formulation shares the geometrical property of Clebsch potentials (e.g. Lamb 1932) for inviscid flows, namely that intersections of different vortex surfaces from independent ϕ_0, can represent vortex lines. This provides a possible approach for the study of the evolution of vortex lines in simple viscous flows.

4.2. *Evolution of VSFs in KP flows*

The evolution of iso-surfaces of the VSF in the KP flow at $Re = 200$ is shown in figure 13 within a subdomain $\pi/2 \leqslant x \leqslant 3\pi/2$ and $0 \leqslant y, z \leqslant \pi$. The vortex surfaces in other subdomains have the same dynamics but move in different directions under the KP symmetries (Kida 1985). In contrast to the initial vortex surfaces for the TG flow in figure 5(*a*), in the KP flow the vortex lines on neighbouring vortex surfaces have the same direction in figure 13(*a*). Again appealing to an interpretation of the

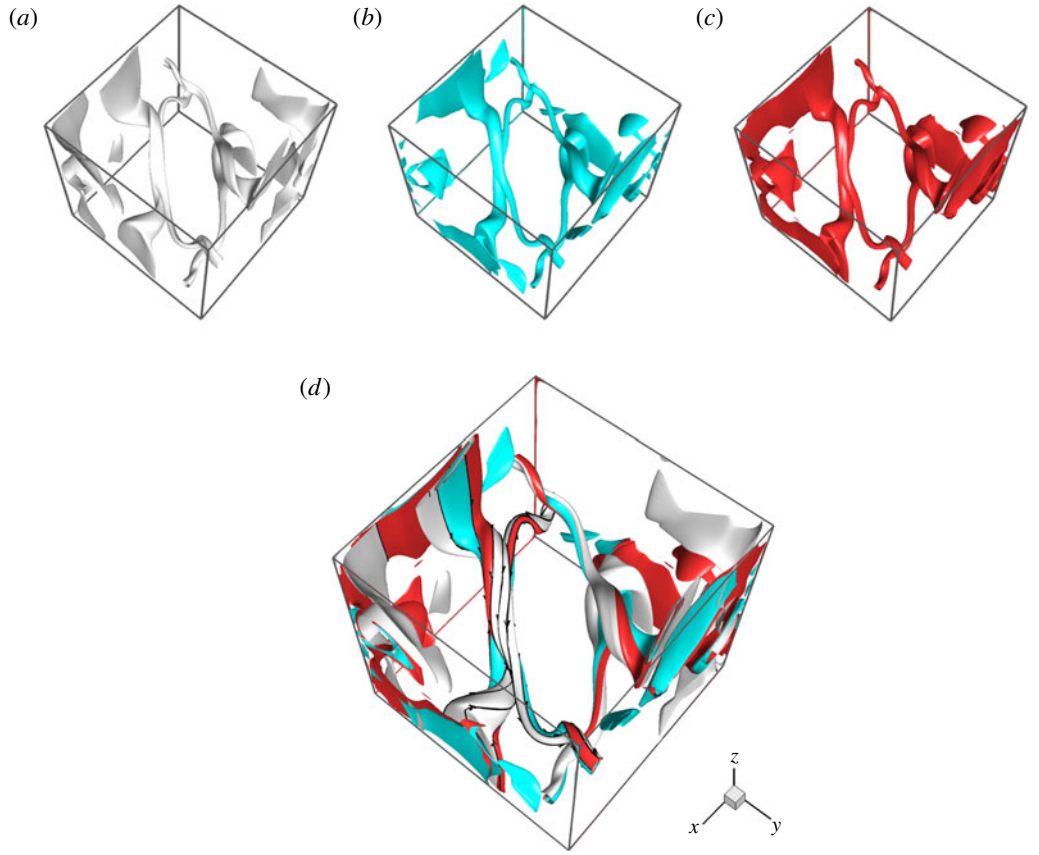

FIGURE 12. (Colour online) Vortex surfaces from three independent initial VSFs (white, $\phi_0 = (\cos 2x - \cos 2y)\cos z$; light blue, $\phi_0 = \cos x \cos y \cos z$; red, $\phi_0 = \cos x \cos^3 y \cos^2 z$) in the TG flow for $Re = 400$ at $t = 7.5$. The surfaces are shown in the subdomain $0 \leqslant x, y, z \leqslant \pi$: (*a*) $\phi_0 = (\cos 2x - \cos 2y)\cos z$, (*b*) $\phi_0 = \cos x \cos y \cos z$, (*c*) $\phi_0 = \cos x \cos^3 y \cos^2 z$. (*d*) Composite structure of vortex surfaces from three independent ϕ_0 shown in figures 12(*a–c*). Some vortex lines are integrated and plotted on the surfaces, in particular, on the intersections between different vortex surfaces from independent ϕ_0.

sense of the velocities induced by the Biot–Savart law indicates that all the vortex surfaces are wound in the same direction and rotate with the z-axis at the centre. This produces the predominant large-scale spiral signatures for the vortex surfaces in the KP flow. In the structural evolution, eight head-to-tail connected vortex surfaces initially form a ring and the blob-like vortex surfaces are progressively distorted into two types of shell-like shapes prior to vortex reconnection (Yang & Pullin 2010). As shown in figure 13(*d*), rolled-up structures appear at the edge of vortex surfaces in the evolution. The neighbouring vortex surfaces are reconnected around $t = 2$ in figure 13(*e*) and stretched structures with complicated geometries are generated at the joint of vortex surfaces at the later stage in figure 13(*f*). The evolutionary geometry of vortex surfaces in both TG and KP flows clearly reveal a scale cascade from large scales with blob-like geometry to small scales with tube-like or sheet-like geometry in the breakdown process.

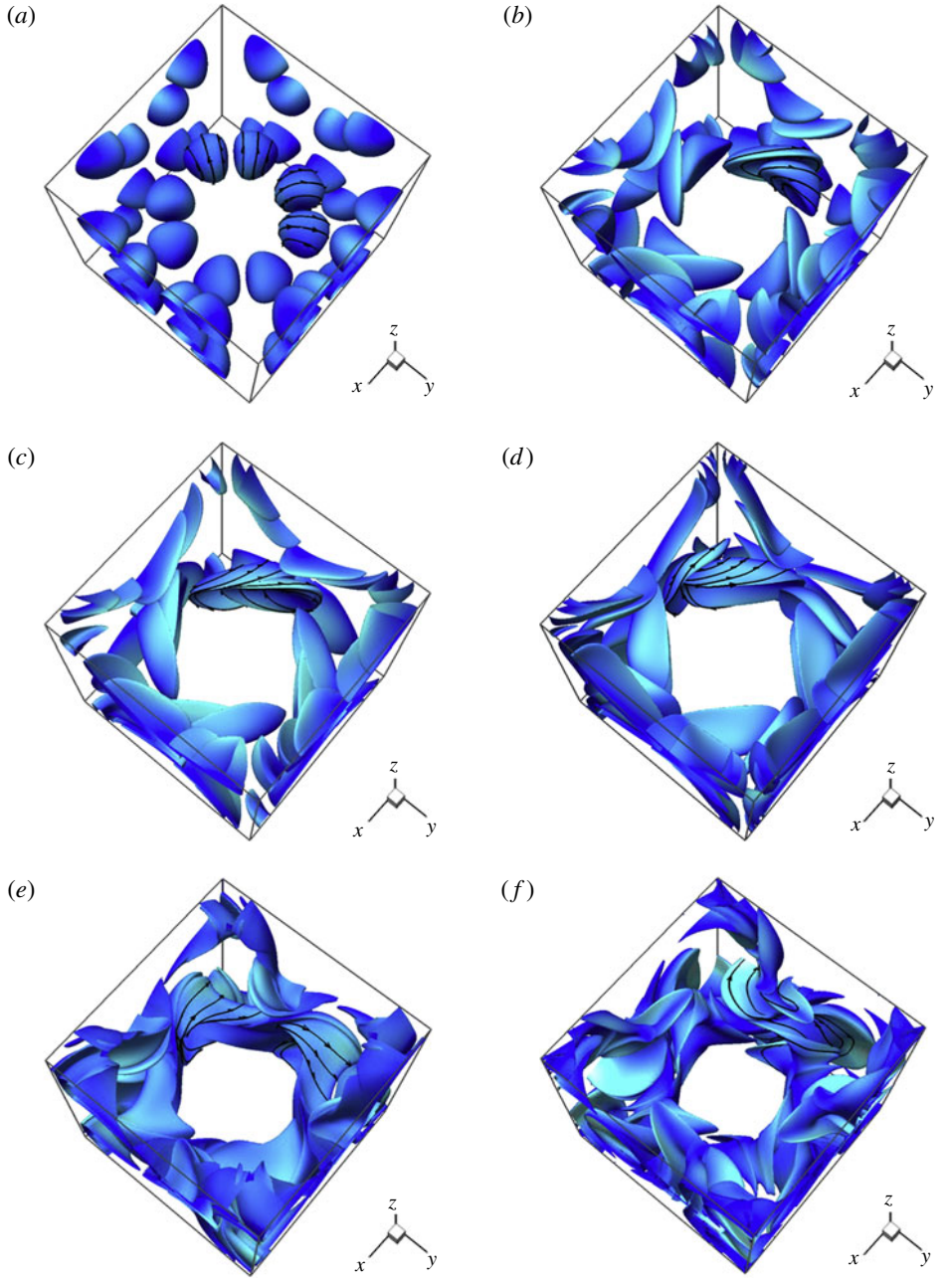

FIGURE 13. (Colour online) Evolution of the VSF in the KP flow at $Re = 200$. Some vortex lines are integrated and plotted on the iso-surfaces at $\hat{\phi}_v$. Colour on the surfaces is rendered by $0 \leqslant |\boldsymbol{\omega}| \leqslant 15$ from blue to red: (*a*) $t = 0$, $\hat{\phi}_v = \pm 0.15$, (*b*) $t = 0.5$, $\hat{\phi}_v = \pm 0.15$, (*c*) $t = 1.0$, $\hat{\phi}_v = \pm 0.15$, (*d*) $t = 1.5$, $\hat{\phi}_v = \pm 0.1$, (*e*) $t = 2.0$, $\hat{\phi}_v = \pm 0.05$, (*f*) $t = 2.5$, $\hat{\phi}_v = \pm 0.025$.

5. Conclusions

In the present study, we have developed a numerical method for computing VSF evolution in some simple viscous incompressible flows. Our starting point is the

expansion of the space of independent coordinates of a set of equations that formally describe the temporal evolution of a VSF, to an extended domain containing a pseudo-time coordinate. This appears to restore uniqueness to the otherwise indeterminate initial-boundary value problem and can be interpreted as a correction step on the original VSF governing equations (Yang & Pullin 2010). There is then some similarity with generic level set methodologies (e.g. Osher & Fedkiw 2003). In the absence of a physical diffusion term, by analogy to the scalar advection equation describing a Lagrangian field, solutions of the extended equation set for VSFs are expected to develop exponentially small scales in the long pseudo-time limit. In numerical implementation, this is handled at present through regularization provided by the implicit numerical dissipation inherent in the numerical WENO scheme used. Our numerical method shows satisfactory convergence in terms of the pseudo-time up to an error threshold that is a function of the grid resolution used for the VSF equations. In addition to the WENO method, other regularization methods could be considered in future work.

The present scheme has been applied in TG and KP flows for real-time periods such that the L_∞ error norm remains at a level sufficiently small that smoothed vortex surfaces, obtained as iso-surfaces of the continuous VSFs, can be extracted. The simulation durations are long enough to reveal the continuous evolutionary geometry of vortex-surface evolution motion from smooth, laminar-like behaviour flows through a 'transition' to a turbulent-like state. The signature of this transition is the onset of topological and geometrical changes in the vortex-surface structure. Pictorially this corresponds to some typical scenarios of vortex dynamics in turbulence, e.g. the collapse of vortex surfaces and vortex reconnection, rolling-up of vortex tubes, vorticity intensification between anti-parallel vortex tubes, and vortex stretching and twisting. For further quantification, the multi-scale geometric diagnostic methodology of Bermejo-Moreno & Pullin (2008) could be useful for characterizing the evolutionary geometry and topology of VSFs (see Yang & Pullin 2010). We expect that higher numerical resolution and Reynolds number would be needed for this than is utilized at present.

We have illustrated the present theory and numerical approach with VSF evolution for simple viscous flows with strong symmetries. It would be of interest to investigate the evolution of VSFs in other simple flows, e.g. vortex rings (e.g. Kida *et al.* 1991) and perturbed vortex tubes (e.g. Hussain & Duraisamy 2011), in particular, at high Reynolds numbers. The computational cost of the correction step in pseudo-time with the current algorithm occupies the major part in the simulation. In order to be applied generally to more complex vortical flows, a technique for accelerated convergence in pseudo-time would probably be required both for generating an initial VSF from a given initial vorticity field and also for tracking the subsequent VSF evolution. Without this the present method has limitations in providing a viable alternative to existing schemes for the purposes of generic, instantaneous flow visualization.

Our approach nevertheless enables, in a novel way, the observation of the timewise evolution of smoothed VSFs in viscous flows, which, to the best of our knowledge, has hitherto been thought to have no well-defined dynamical meaning as an initial-boundary value problem. For this reason alone the application of the present algorithm to special cases of interesting canonical flows, at some computational cost, may be justified. In addition, relevant topological methods based on contact structures (Ghrist & Komendarczyk 2002) or vector segments (Wang 2010) might be useful to improve the current methodology for more general flows.

Finally, we remark that globally smoothed VSFs may not exist in general flows when the vorticity field is not integrable, in which case a surrogate field with acceptably small $\langle|\lambda_\omega|\rangle$ could perhaps be obtained by using (2.18).

This work has been supported in part by the National Science Foundation under grant DMS-1016111.

REFERENCES

BATCHELOR, G. K. 1967 *An Introduction to Fluid Dynamics*. Cambridge University Press.

BERMEJO-MORENO, I. & PULLIN, D. I. 2008 On the non-local geometry of turbulence. *J. Fluid Mech.* **603**, 101–135.

BORATAV, O. N. & PELZ, R. B. 1994 Direct numerical simulation of transition to turbulence from a high-symmetry initial condition. *Phys. Fluids* **6**, 2757–2784.

BRACHET, M. E., MEIRON, D. I., ORSZAG, S. A., NICKEL, B. G., MORF, R. H. & FRISCH, U. 1983 Small-scale structure of the Taylor–Green vortex. *J. Fluid Mech.* **130**, 411–452.

CHEN, S., EYINK, G. L., WAN, M. & XIAO, Z. 2006 Is the Kelvin theorem valid for high Reynolds number turbulence? *Phys. Rev. Lett.* **97**, 144505.

CONSTANTIN, P., PROCACCIA, I. & SEGEL, D. 1995 Creation and dynamics of vortex tubes in three-dimensional turbulence. *Phys. Rev.* E **51**, 3207–3222.

CRANDALL, M. G. & LIONS, P. L. 1983 Viscosity solutions of Hamilton–Jacobi equations. *Trans. Am. Math. Soc.* **277**, 1–42.

FUKUMOTO, Y. & OKULOV, V. L. 2005 The velocity field induced by a helical vortex tube. *Phys. Fluids* **17**, 107101.

GHRIST, R. & KOMENDARCZYK, R. 2002 Topological features of inviscid flows. In *Introduction to the Geometry and Topology of Fluid Flows*, *NATO–ASI Series II, vol. 47*, pp. 183–202. Kluwer.

HELMHOLTZ, H. 1858 Über Integrale der Hydrodynamischen Gleichungen Welche den Wirbelbewegungen Entsprechen. *J. Reine Angew. Math.* **55**, 25–55.

HUSSAIN, F. & DURAISAMY, K. 2011 Mechanics of viscous vortex reconnection. *Phys. Fluids* **23**, 021701.

JEONG, J. & HUSSAIN, F. 1995 On the identification of a vortex. *J. Fluid Mech.* **285**, 69–94.

JIANG, G. S. & SHU, C. W. 1996 Efficient implementation of weighted ENO schemes. *J. Comput. Phys.* **126**, 202–228.

JIMENEZ, J., WRAY, A. A., SAFFMAN, P. G. & ROGALLO, R. S. 1993 The structure of intense vorticity in isotropic turbulence. *J. Fluid Mech.* **255**, 65–90.

KERR, R. M. 1993 Evidence for a singularity of the three-dimensional, incompressible Euler equations. *Phys. Fluids* A **5**, 1725–1746.

KIDA, S. 1985 Three-dimensional periodic flows with high-symmetry. *J. Phys. Soc. Japan* **54**, 2132–2136.

KIDA, S. & TAKAOKA, M. 1994 Vortex reconnection. *Annu. Rev. Fluid Mech.* **26**, 169–189.

KIDA, S., TAKAOKA, M. & HUSSAIN, F. 1991 Collision of two vortex rings. *J. Fluid Mech.* **230**, 583–646.

LAMB, H. 1932 *Hydrodynamics*, 6th edn. Cambridge University Press.

MINGYU, H., KÜPPER, T. & MASBAUM, N. 1997 Computation of invariant tori by the Fourier methods. *SIAM J. Sci. Comput.* **18**, 918–942.

OHKITANI, K. & CONSTANTIN, P. 2003 Numerical study of the Eulerian–Lagrangian formulation of the Navier–Stokes equations. *Phys. Fluids* **15**, 3251–3254.

OSHER, S. & FEDKIW, R. 2003 *Level Set Methods and Dynamic Implicit Surfaces*. Springer.

PULLIN, D. I. & SAFFMAN, P. G. 1998 Vortex dynamics in turbulence. *Annu. Rev. Fluid Mech.* **30**, 31–51.

RICCA, R. L. 1994 The effect of torsion on the motion of a helical vortex filament. *J. Fluid Mech.* **273**, 241–259.

SAFFMAN, P. G. 1992 *Vortex Dynamics*. Cambridge University Press.

SHE, Z. S., JACKSON, E. & ORSZAG, S. A. 1990 Intermittent vortex structures in homogeneous isotropic turbulence. *Nature* **344**, 226–228.

SHU, C. W., DON, W. S., GOTTLIEB, D., SCHILLING, O. & JAMESON, L. 2005 Numerical convergence study of nearly incompressible, inviscid Taylor–Green vortex flow. *J. Sci. Comput.* **24**, 569–595.

SIGGIA, E. D. 1985 Collapse and amplification of a vortex filament. *Phys. Fluids* **28**, 794–805.

TAYLOR, G. I. & GREEN, A. E. 1937 Mechanism of the production of small eddies from large ones. *Proc. R. Soc. Lond.* A **158**, 499–521.

TRUESDELL, C. 1954 *The Kinematics of Vorticity*. Indiana University Press.

WANG, L. 2010 On properties of fluid turbulence along streamlines. *J. Fluid Mech.* **648**, 183–203.

YANG, Y. & PULLIN, D. I. 2010 On Lagrangian and vortex-surface fields for flows with Taylor–Green and Kida–Pelz initial conditions. *J. Fluid Mech.* **661**, 446–481.

YANG, Y. & PULLIN, D. I. 2011 Geometric study of Lagrangian and Eulerian structures in turbulent channel flow. *J. Fluid Mech.* **674**, 67–92.

YANG, Y., PULLIN, D. I. & BERMEJO-MORENO, I. 2010 Multi-scale geometric analysis of Lagrangian structures in isotropic turbulence. *J. Fluid Mech.* **654**, 233–270.